Welding in the World (2022) 66:1213–1227
https://doi.org/10.1007/s40194-022-01296-3

RESEARCH PAPER

Microstructure and Impact Toughness of the Coarse-Grain HAZ Physically Simulated with Different Heat Inputs in a 690 MPa Ultra-low Carbon High-Strength Microalloyed Steel

Yulong Yang[1] · Xiao Jia[2] · Yaxin Ma[2] · Ping Wang[1] · Fuxian Zhu[2]

Received: 7 December 2021 / Accepted: 28 March 2022 / Published online: 2 April 2022

Abstract
An ultra-low carbon steel plate with the yield strength of 690 MPa was produced in the laboratory. The coarse-grain heat-affected zone (CGHAZ) was simulated on a thermal simulator based on the welding heat inputs of 25 kJ/cm and 100 kJ/cm, under which the microstructure and impact toughness were characterized compared with the base metal (BM). The results showed that the investigated steel exhibited a favorable low-temperature impact toughness at the heat input of 25 kJ/cm. Although high heat input was not conducive to the impact toughness, the average impact energy can still reach ~40 J at − 20℃ at the heat input of 100 kJ/cm. The welding thermal cycle led to the formation of more low-angle boundaries in the prior austenite grains, which was not conducive to the crack arrest behavior, resulting in a significant decrease of toughness in CGHAZ. Obvious decrease of high-angle boundaries in CGHAZ was mainly responsible for the deterioration of total impact absorbed energy. Besides, the martensite-austenite (M-A) constituents provided favorable conditions for crack initiation. In general, the mechanism of impact toughness deterioration of CGHAZ under high heat input condition was discussed in detail. The microstructure and low-temperature impact toughness of CGHAZ under different heat inputs can provide a theoretical basis for the research in 690 MPa ultra-low carbon high-strength microalloyed steels.

Keywords High heat input · CGHAZ · M-A constituents · Impact toughness · High-angle boundaries

1 Introduction

In recent years, high-strength low-carbon microalloyed steels used for high heat input welding have been widely used in bridge construction, ocean engineering, and other fields [1, 2]. Although the welding efficiency is improved by high heat input welding technology, the significant decrease of toughness in coarse-grain heat-affected zone (CGHAZ) due to the high heat input has always been an issue of concern [3–5]. Therefore, the mechanism of toughness deterioration in CGHAZ and the relationship between microstructure and impact toughness under high heat input welding conditions of high-strength low-carbon microalloyed steel have been attracting much attention [6].

As is known, the microstructure of base metal (BM) has an important effect on the weldability. Gordienko et al. studied the effect of the initial microstructure of X70 steel on the mechanical properties of heat-affected zone (HAZ) and pointed out that the BM with refined microstructure is beneficial to reduce the brittleness of welded joints [7]. In addition, the strength of BM is one of the important factors affecting the weldability. For steels with a yield strength less than 550 MPa, the microstructure of CGHAZ is mainly composed of acicular ferrite. Xiong et al. studied the influence of acicular ferrite on the crack initiation and propagation in CGHAZ and pointed out that the presence of acicular ferrite improves the impact toughness effectively because the acicular ferrite as a plastic phase is composed of massive interlocking high-angle boundaries, which has greater potential to absorb external impact energy and retards the crack propagation [8]. Besides, Wan and Wang et al. also

Recommended for publication by Commission X - Structural Performances of Welded Joints - Fracture Avoidance

✉ Ping Wang
wang20211107@126.com

[1] Key Laboratory of Electromagnetic Processing of Materials, Ministry of Education, Northeastern University, Shenyang 110819, China

[2] State Key Laboratory of Rolling and Automation, Northeastern University, Shenyang 110819, China

indicated that the acicular ferrite with high-angle boundaries is chaotic with other microstructure to separate the austenite grains, which promotes the grain refinement and improves the toughness of CGHAZ [9, 10]. It can be seen that the positive effect of high fraction of acicular ferrite on the impact toughness of CGHAZ is undoubted.

However, as the strength of BM increases, the microstructure of CGHAZ will inevitably change after being subjected to the welding thermal cycle especially under high heat input conditions [11, 12]. Due to the high strength of the BM, the acicular ferrite with high-angle boundaries in CGHAZ is reduced and replaced by more lath bainite or granular bainite, etc., which has different effect on the crack initiation and propagation [13, 14]. Hu et al. conducted the welding thermal simulation of 590 MPa high-strength low-carbon microalloyed steel with different heat inputs and pointed out that with the increase of heat input, the microstructure of CGHAZ gradually transforms from lath martensite to granular bainite or even boundary ferrite, which significantly reduces the impact toughness of CGHAZ [4]. In addition, Lan et al. also demonstrated that the microstructure in CGHAZ of 690 MPa high-strength low-carbon microalloyed steel can transform from lath martensite to coarse lath bainite under high heat input welding conditions [15]. Cui et al. also pointed out that for 890 MPa high-strength low-carbon microalloyed steel, the microstructure of CGHAZ is mainly composed of lath martensite or bainite at low high heat input. The low-angle boundaries in the coarse lath bainite clusters can not effectively inhibit the crack propagation, which leads to the larger cleavage planes [16]. Therefore, the higher strength of the BM, the more unfavorable microstructure of CGHAZ is to the impact toughness with different heat inputs. Besides, more boundary microstructure will also be formed inevitably due to the greater driving force under high heat input condition. The martensite-austenite (M-A) constituents and boundary microstructure are considered as the main affecting factors for the crack initiation and propagation, which are the main reasons for the decrease of toughness in CGHAZ [13, 17]. Relevant references pointed out that the M-A constituents as brittle phases, contribute greatly to the nucleation of microcracks and reduce the crack initiation energy [18]. Besides, the larger size of M-A constituents may contribute more to the total impact energy than the coarse austenite grains, because the greater the size of M-A constituent is, the larger the stress concentration at the interface with the matrix accumulates, which provides more easier crack initiation sources to form large cleavage planes [18–20]. Lambert-Perlade et al. studied the formation of cracks in CGHAZ of 550 MPa high-strength low carbon microalloyed steel and found that, although the high-angle boundaries always play an inhibiting role in crack propagation, both the M-A constituents and boundary microstructure (such as upper bainite) are harmful to the impact toughness, and the crack initiation is mainly related to the stress–strain state at the interface between M-A constituents and matrix [21]. In addition, Ramachandran et al. also pointed out that under high heat input conditions, the carbon atoms in the residual austenite tend to segregate towards the grain boundaries to form the M-A constituents in high-strength low-carbon microalloyed steels, and the M-A constituents and the coarse boundary microstructure together decrease the toughness of CGHAZ [22]. In addition, the higher strength of BM means that the carbon equivalent is increased, which provides favorable conditions for the formation of M-A constituents in CGHAZ. Therefore, the ultra-low-carbon alloying design seems to deserve much attention.

Although the mechanism of toughness reduction of CGHAZ has attracted much attention, there are few studies mainly focusing on the steel of ultra-low-carbon alloying design with the yield strength more than 690 MPa under high heat input of 100 kJ/cm. It should be pointed out that despite the similar high-strength, the microstructure of CGHAZ still varies greatly at different heat inputs, which is directly related to the microstructure and alloy composition of BM. In this paper, a steel plate of ultra-low-carbon microalloyed design with the yield strength of 690 MPa was investigated. To make it easier to study the CGHAZ under low and high heat inputs, the welding thermal simulation was carried out based on the heat inputs of 25 kJ/cm and 100 kJ/cm. By analyzing the microstructure and impact toughness of the BM and simulated CGHAZ, the relationship between microstructure and impact toughness was studied and the mechanism of fracture in CGHAZ under high heat input was discussed in detail, which provides a theoretical basis for improving the toughness of CGHAZ in 690 MPa ultra-low-carbon high-strength microalloyed steels.

2 Materials and methods

The investigated steel was melted using a vacuum induction heating furnace in the laboratory. The clean iron bars were used as the basic steel and the whole process of the deoxidation was carried out with less Al addition. The main alloy adding order was as follows: Mn iron–Si iron–Al/Ti iron–other microalloys. The elements such as Cr, Ni, Mo, and Cu were initially added along with the raw iron bars. The surface vacuum during the melting process was about 100 Pa. The weight of the ingot was about 20 kg. After removal of the heads and tails as well as austenitic homogenization at 1250℃ for 6 h, the ingots were forged into square billets with the size of 80 mm × 80 mm. To ensure the width was not less than 80 mm, the length direction of the billet was freely extended. The actual chemical composition of the investigated steel are shown in Table 1:

Table 1 Actual chemical composition of the investigated steels (wt%)

C	Si	Mn	Al	≤P	≤S	≤V,Ti	Mo	Cr	Ni	Cu
0.04	0.185	1.681	0.011	0.009	0.0073	0.431	0.293	0.823	0.812	0.011

The square billet was heated to 1250℃ holding for 6 h in a furnace again and then rolled on a Ø450 × 450 Two-high Reversing Hot Mill. Traditional two-stage rolling process called thermal mechanical control processing (TMCP) technology was used to obtain the BM. The initial and final rolling temperature was controlled in the range of 1100~1150℃ and 850~900℃, respectively. After the second stage of rolling process, the plate was quickly cooled by water to room temperature. The final thickness of the plate was 13 mm. After cooling to room temperature, the quenched plate was tempered at 450℃ for 1 h in a vacuum heating furnace. The basic mechanical properties of BM are as follows: yield strength at room temperature: ~729 MPa; tensile strength at room temperature: ~833 MPa; impact toughness at − 20℃: ~175 J; uniform elongation at room temperature: ~12.5%. It can be seen that the mechanical properties of the investigated steel meet the commercial base material index of 690 MPa grade steel. The only drawback is that the uniform elongation (~12.5%) is slightly lower than the industrial requirement (industrial requirement ≥ 14%). However, from the perspective of welding thermal cycle, the difference of 1.5% in uniform elongation does not seem to affect the evaluation of the microstructure and performance of CGHAZ. The laboratory milling treatment was carried out to correspond with commercial base material to the maximum extent to ensure the sufficient strength of BM without loss of toughness.

For the convenience of studying CGHAZ, the specimen with the size of 11 mm × 11 mm × 55 mm was machined from the middle of the tempered plate along the rolling direction. The welding thermal simulation was carried out on a Gleeble-3800 thermal simulator. The Rykalin-2D curve model was used to output corresponding $t_{8/5}$ (the cooling time from 800 to 500℃ during the welding thermal cycle) value by certain heat input [3, 4, 15]. The simulated welding heat input was 25 kJ/cm and 100 kJ/cm, respectively. In the process of welding thermal simulation, two thermocouples with a distance of 5 mm were welded at the center of the specimen. The specimen subsequently was heated from 25 to 1400℃ at the heating rate of 80℃/s and kept for 1 s, then cooled to 350℃ under different cooling rates based on heat inputs of 25 kJ/cm and 100 kJ/cm. The simulated thickness was 60 mm, and the corresponding time of $t_{8/5}$ was about 32 s and 139 s. The welding thermal simulation parameters mentioned above were based on the electro-gas welding (EGW) process in the trial production of the investigated steel. The equivalent practical application and process with the high heat inputs are showing in Table 2.

Table 2 Actual welding parameters equivalent to the welding thermal simulation

Current type	Current (A)	Voltage (V)	Welding speed (cm/min)	Preheating temperature (℃)	Heat input (kJ/cm)
DCEP	530	32	39.5	25	25.8
DCEP	550	38	12.6	25	99.5

Heat input (kJ/cm) = current (A) × voltage (V) × 60/welding speed (cm/min)/1000

DCEP direct current electrode positive

The specimens were machined into the size of 10 mm × 10 mm × 55 mm with a V-notch in the middle. Charpy impact test was carried out at − 20℃ on an instrumented impact testing machine (NI750C) according to the international standard ISO 148–1. The detailed energy absorption during crack initiation and propagation can be obtained by the instrumented impact test.

In situ observation of the prior austenite grains and the phase transformation during welding thermal cycle was carried out by a high-temperature confocal laser scanning microscope (CLSM). The size of the specimens was Ø7 × 3 mm, and the thermal cycle parameters were consistent with the welding thermal simulation. Optical microscope (OM) and scanning electron microscope (SEM) were used to analyze the metallographic microstructure and fracture morphology. After the samples were polished, the LePera reagent (equal ratio of 4 gm picric acid in 100 methyl alcohol + 1 g Na2S2O5 in 100 ml water, etched for 20 s) was used to characterize the M-A constituents [22]. Crystallographic characteristics was analyzed using a field emission scanning electron microscope (FE-SEM ZEISS Ultra-55) equipped with EBSD technology based on the step size of 0.5 μm. The HKL Channel 5 software was used for data processing. In order to remove the surface stress layer, the samples used for EBSD analysis were prepared by an electrochemical polishing equipment with the voltage of 20 V. The electrolyte was 12.5% perchlorate alcohol solution, the electrolytic time was 20 s, and the electrolytic temperature was 25℃. A field emission transmission electron microscope (TEM) with output voltage of 200 keV was used to observe the submicrostructure and precipitates. The film specimens were prepared by an twin-jet electropolisher (TENUpol-5) with the voltage of 50 V. The electrolyte was a 10%

perchlorate alcohol solution, and the electrolytic temperature was – 20℃.

3 Results

3.1 Microstructure and Phase Transformation

Figure 1 shows the optical microstructure of BM and simulated CGHAZ based on heat inputs of 25 kJ/cm and 100 kJ/cm. It can be seen from Fig. 1a that the microstructure of BM is dominated by tempered lath bainite (TLB) with incomplete precipitation of carbides. Obvious elongated austenite grains along the rolling direction indicate the effect of TMCP technology on the austenite grains. After welding thermal cycle, the optical microstructure of the simulated CGHAZ changes significantly no matter in the CGHAZ-25kJ/cm or CGHAZ-100kJ/cm specimen. The lath bainite decreases and the granular bainite increases gradually as shown in Fig. 1b and c. Compared with the CGHAZ-25kJ/cm specimen, the difference of CGHAZ-100kJ/cm specimen is that the granular bainite is dispersed, and the lath bainite is almost absent. Besides, the prior austenite grains are coarse obviously and present a polygon shape after being subjected to high heat input welding thermal cycle as shown in Fig. 1c.

Figure 2 shows the in situ observation of phase transformation in simulated high heat input CGHAZ of 100 kJ/cm based on CSLM technology. As can be seen, the initial temperature of phase transformation occurs at about ~593℃, which is the typical transformation region for bainite. With the decrease of temperature, different degree of bainite transformation occurs in the austenite grains. The variation of phase transformation in the blue dotted grains in the figures shows that the bainite transformation process is controlled by the typical shear mechanism. Besides, large fraction of bainite nucleation are observed not only at the prior austenite grain boundaries but also at the new grain boundaries of the primary bainite laths. It can also be found that the average diameter of austenite grains is more than 100 μm and the size of austenite grains is not uniform during the cooling process. This is basically consistent with the experimental results in Fig. 1c, which shows the phase transformation behavior during the cooling stage of welding thermal cycles.

3.2 Impact Test and Crack

Figure 3 shows the average impact energy and the typical impact load–deflection curves of BM and simulated CGHAZ. As can be seen from Fig. 3a, the average impact energy of BM is ~175 J at – 20℃. With the increase of the heat input, the impact absorption energy decreases gradually. The value only decreases slightly from ~175 to ~140 J after being subjected to heat input of 25 kJ/cm. However, under the conditions of high heat input of 100 kJ/cm, the impact energy of CGHAZ decreases obviously, and the average value is only ~40 J. In addition, the percentage of crack

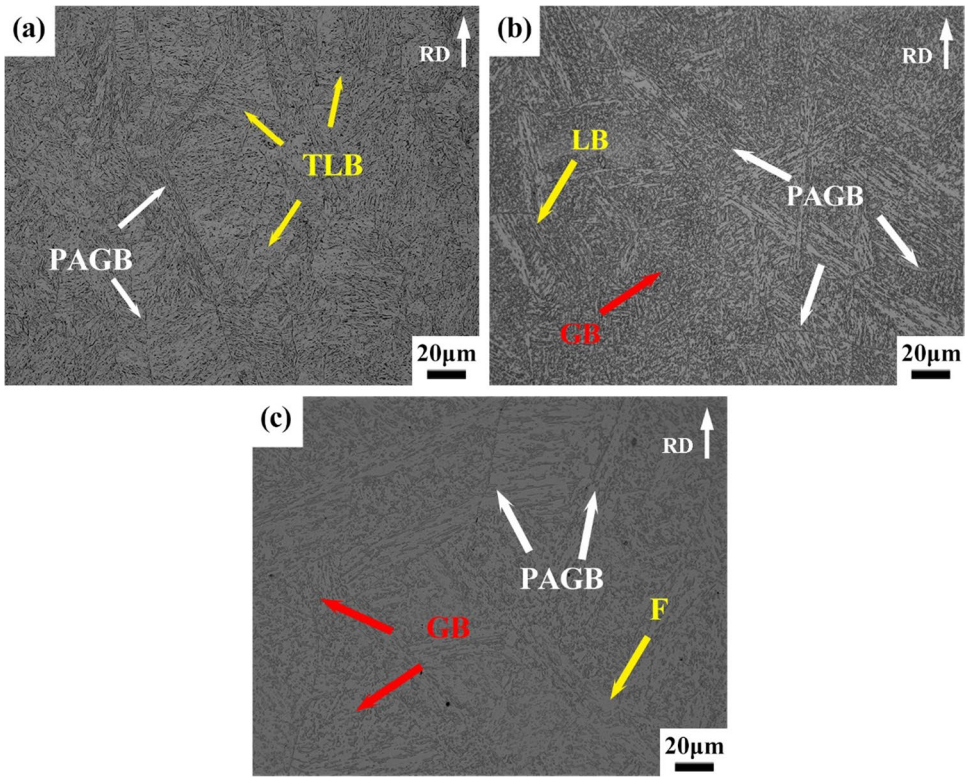

Fig. 1 Optical microstructure of BM and simulated CGHAZ. **a** BM; **b** CGHAZ-25 kJ/cm; **c** CGHAZ-100 kJ/cm. PAGB, prior austenite grain boundary; LB, lath bainite; TLB, tempered lath bainite; GB, granular bainite; F, ferrite; RD, rolling direction

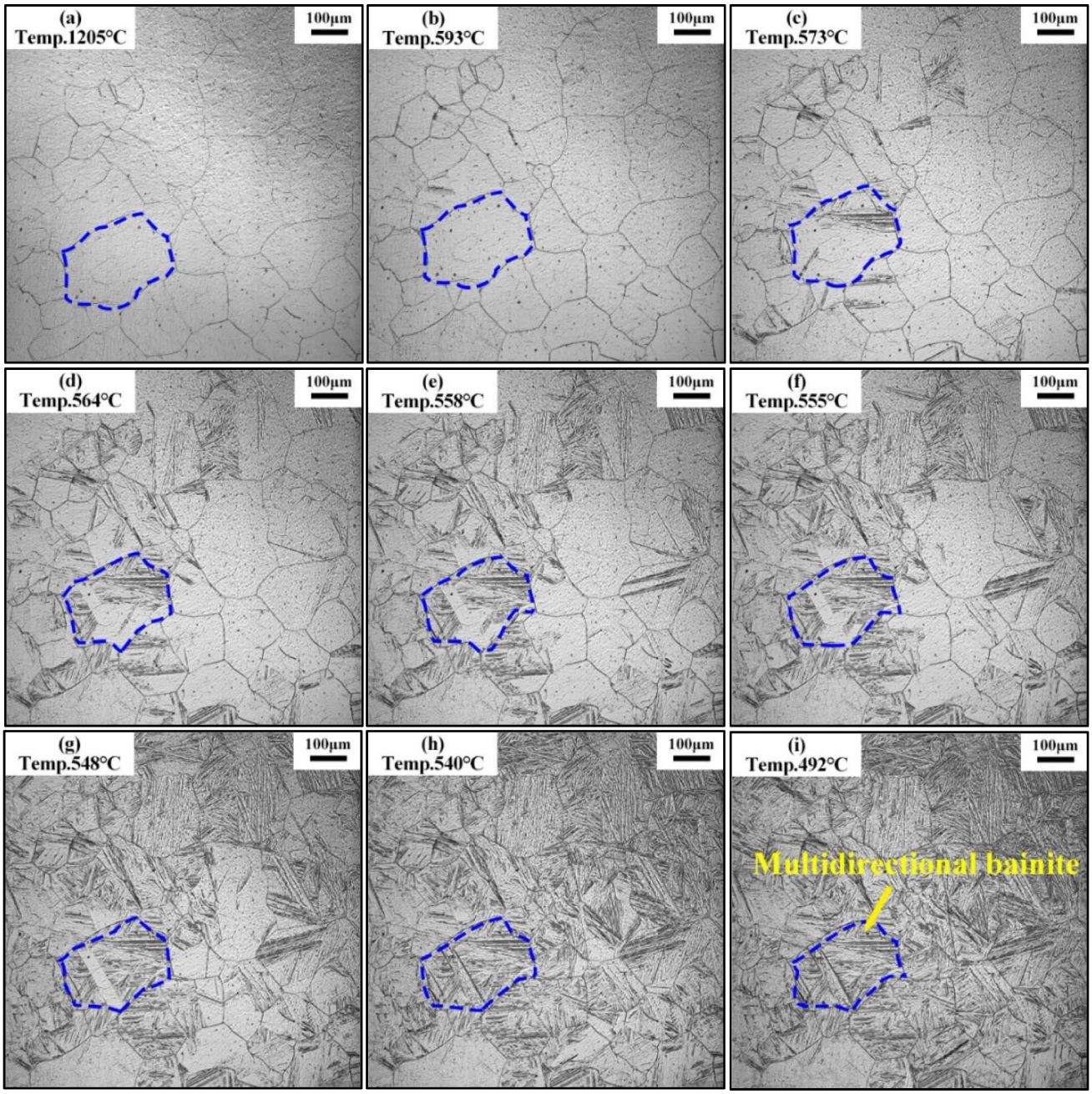

Fig. 2 In situ observation of the phase transformation in simulated high heat input CGHAZ of 100 kJ/cm based on CSLM. **a**–**i** Phase transition temperature points during the temperature drop from 1205 to 492℃. The blue dotted grains in the figures refer to a prior austenite grain, in which the multidirectional bainites are observed

propagation energy in the total impact energy is consistent with the trend of average impact energy in the investigated steel.

The typical load–deflection curves in Fig. 3b–d show that the maximum loading force of BM and CGHAZ can reach ~19.57 kN, ~18.55 kN, and ~14.71 kN, respectively. In the tempered BM, the loading force decreases slowly after reaching its maximum value and always shows a stable downward trend. However, only a slight fluctuation is observed in the decreasing process of loading force of CGHAZ-25 kJ/cm specimen. Compared with the BM and CGHAZ-25 kJ/cm, the maximum loading force of CGHAZ-100 kJ/cm fluctuates to the maximum during the rising process, and then falls rapidly to a stable decreasing stage after an obvious cliff-like drop. The absorbed energy during the crack initiation and propagation process can be reflected by the ascending and

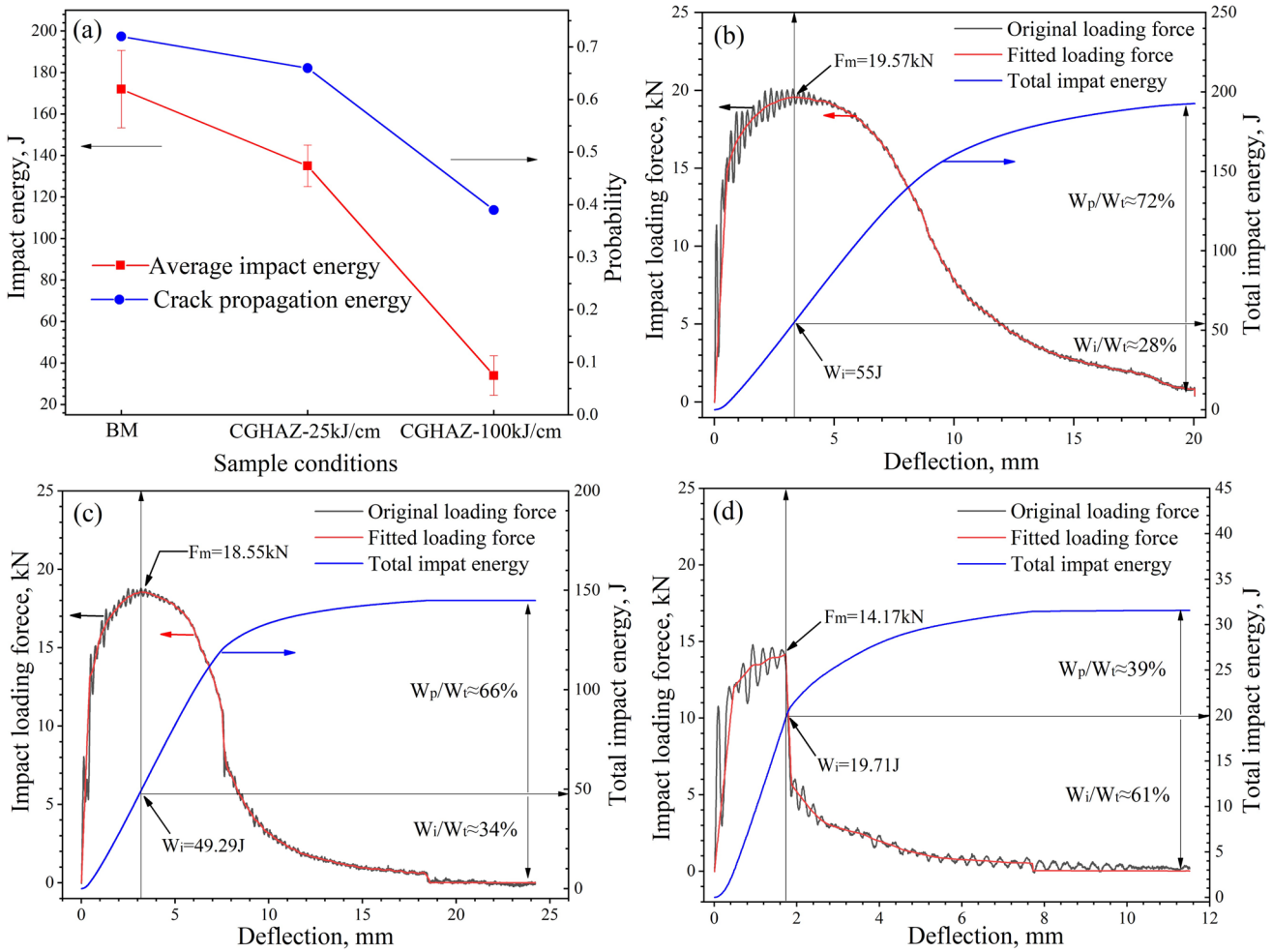

Fig. 3 Impact performance of BM and simulated CGHAZ at − 20℃. **a** Average impact energy and relationship between crack propagation energy and total impact energy. **b–d** Typical impact load–deflection curves of BM (**b**), CGHAZ-25 kJ/cm (**c**), and CGHAZ-100 kJ/cm (**d**). Fm, maximum loading force; Wi/Wp/Wt, crack initiation/propagation/total absorbed energy

descending stages of load–deflection curves. By calculation, the percentage of crack initiation energy to the total impact absorbed energy in BM and CGHAZ-25 kJ/cm is ~28% and ~34%, respectively, which is much smaller than the value of ~63.5% in CGHAZ-100 kJ/cm specimen. However, the tempered BM exhibits a larger crack propagation absorbed energy of ~72% (~66% of CGHAZ-25 kJ/cm and ~36% of CGHAZ-100 kJ/cm). The cliff-like descent stage observed in Fig. 3d suggests that more cleavage planes may be formed at the fracture, which are responsible for the deterioration of the impact toughness. In general, the crack propagation energy is reduced due to the welding thermal cycles, which weakens the total impact energy.

The fractographs of typical tempered BM and the simulated CGHAZ-100 kJ/cm were analyzed, and the results are shown in Fig. 4. It can be seen that the shear lip and tear zone in the macroscopic fractograph of BM are apparent as shown in Fig. 4a. However, in the simulated CGHAZ-100 kJ/cm specimen, the radiation zone covers the entire macroscopic fracture as shown in Fig. 4c. Compared with the simulated CGHAZ-100 kJ/cm, the microscopic fractograph of BM is mainly composed of more dimples instead of typical cleavage planes. In addition, it is noteworthy that inclusions with different shapes and sizes are observed in both the dimples and cleavage planes as shown in Fig. 4b, d, which may provide a favorable condition for crack initiation during the impact process.

The typical microcrack initiation and propagation paths in simulated high heat input CGHAZ-100 kJ/cm can be clearly observed in Fig. 5. As the red dotted line shows, once the initial microcrack has formed, it will be highly likely to induce a secondary crack at the weak locations of the initial microcracks. Besides, the M-A constituents can be used as the microcrack initiation sources in the matrix and promote the crack initiation process as shown in Fig. 5b and c. In addition, it is worth noting that most of the crack

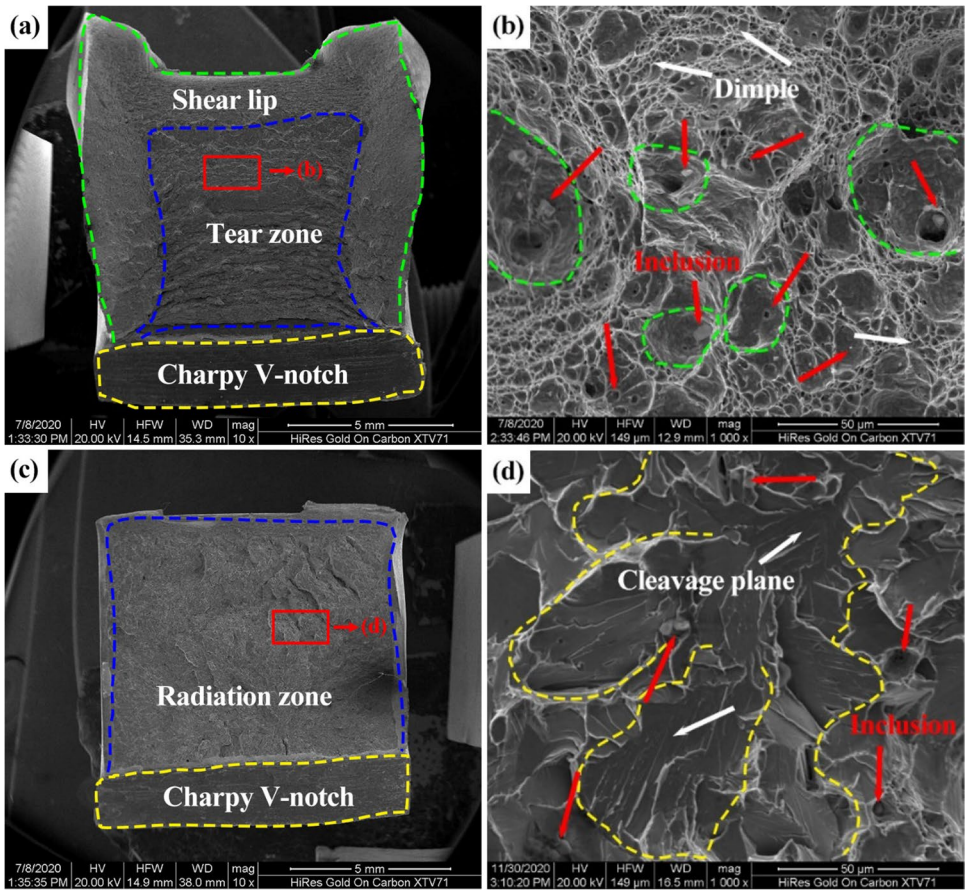

Fig. 4 Typical fractograph of the BM (**a**, **b**) and simulated high heat input CGHAZ-100 kJ/cm (**c**, **d**) based on scanning electron microscopy. **a**, **c** Macroscopic morphologies; **b**, **d** Magnified micro-morphologies in the red solid line squares in **a** and **c**

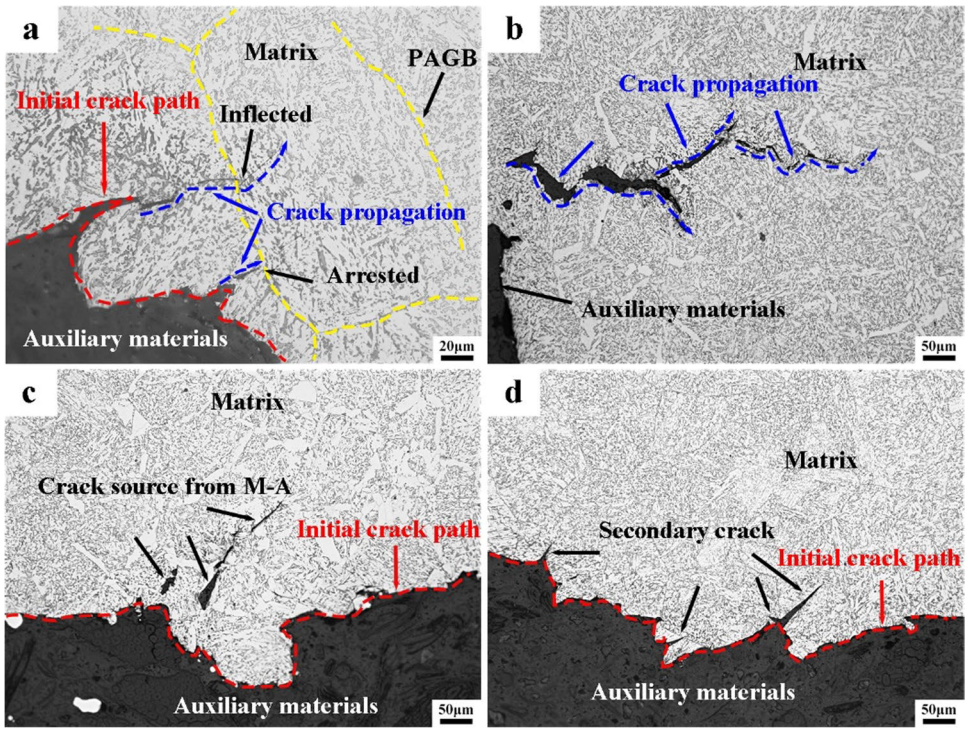

Fig. 5 Crack initiation and propagation paths in the simulated high heat input CGHAZ-100 kJ/cm under optical microscope conditions. PAGB refers to the prior austenite grain boundary. **a**, **b** Deflected crack paths by high-angle boundaries. **c**, **d** Typical transgranular fracture and initiation source of M-A

propagation paths are controlled by transgranular fracture, and the crack propagation paths are deflected by some certain grain boundaries more or less, presenting an arresting effect as shown in Fig. 5a, b.

3.3 Crystallographic Characteristics

Figures 6 and 7 show the distribution of grain boundaries in BM and simulated CGHAZ as well as the quantitative analysis based on EBSD technology. In Fig. 6, the black solid lines indicate that the misorientation is greater than 15°, while the red solid lines indicate that the misorientation is between 5° and 15°. A decreasing frequency of high-angle boundaries greater than 15° in CGHAZ can be observed compared with the BM as shown in Figs. 6 and 7c, d. With the increase of heat input, the high-angle boundaries decrease sharply. However, compared with the BM and CGHAZ-25 kJ/cm, the probability of misorientation less than 15° is higher in CGHAZ-100 kJ/cm and mainly concentrated in the vicinity of 2°. With the increase of misorientation, the distribution probability decreases obviously, especially in the CGHAZ-100 kJ/cm sample, when the misorientation is greater than 15°, the distribution probability shows a significant downward trend.

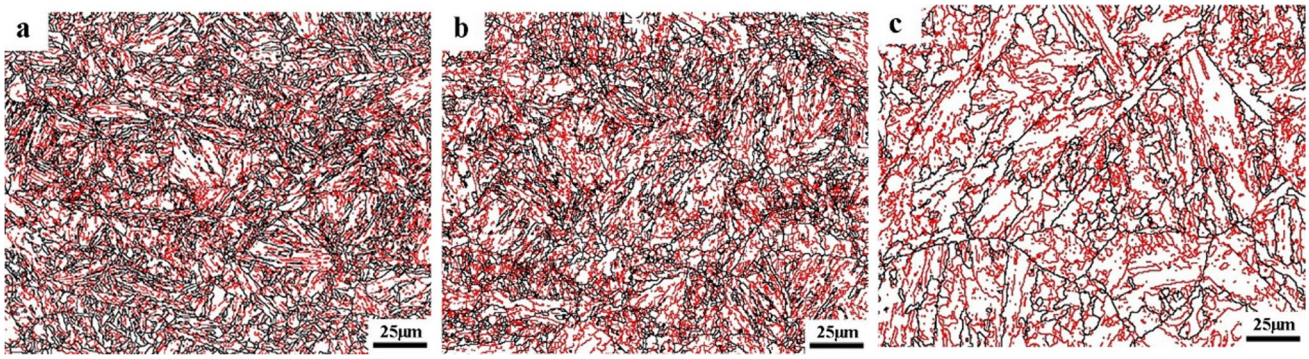

Fig. 6 Grain boundaries of BM and simulated CGHAZ based on EBSD technology. **a** BM; **b** CGHAZ-25 kJ/cm; **c** CGHAZ-100 kJ/cm. The black solid lines indicate the misorientations greater than 15°, and the red solid lines refer to that between 5° and 15°

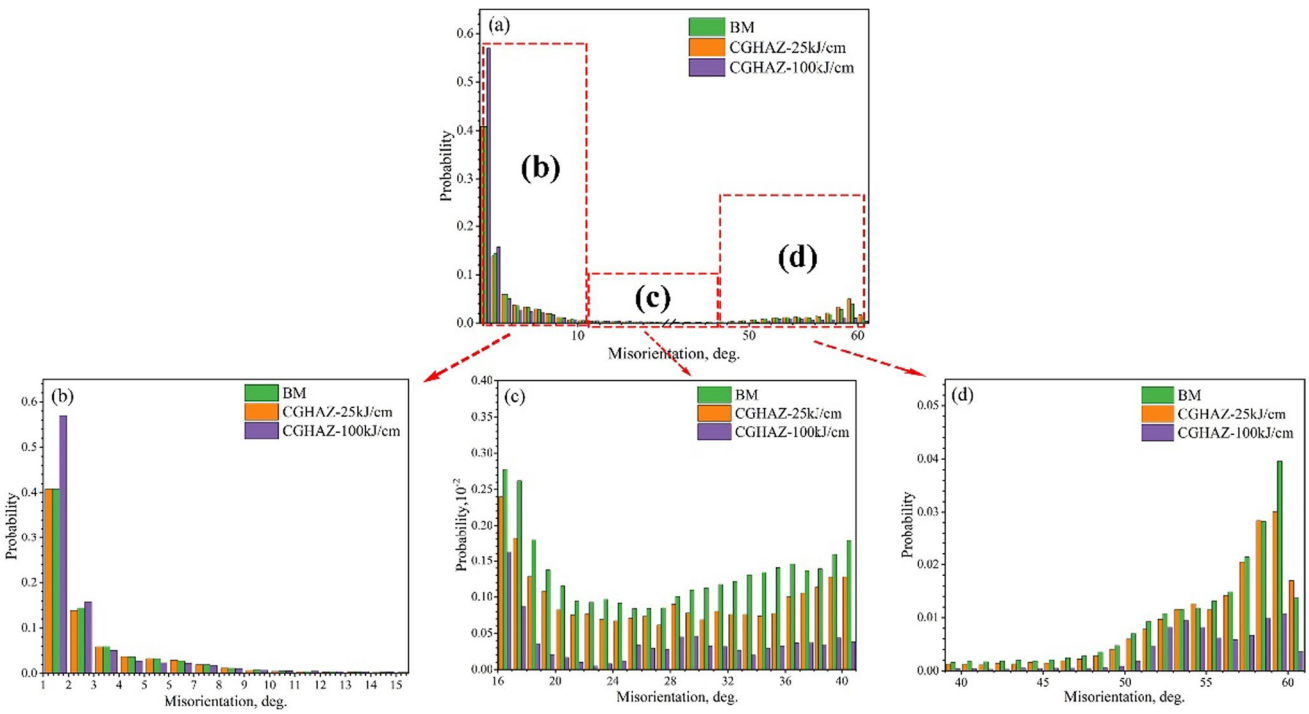

Fig. 7 Quantitative analysis of the grain boundary misorientation in BM and simulated CGHAZ based on EBSD technology. The magnified images in **a** are shown in **b–d**

Figure 8 shows the quantitative statistics of the effective grain size of BM and simulated CGHAZ based on EBSD technology. The effective grains are defined as the boundary misorientation angle ≥ 15°. As can be seen, the probability of greater effective grains (such as the grain diameter of 10 μm 40 μm) becomes more frequent with the increase of heat input. Taking effective grain size of 10 μm as an example, it can be seen that the high probability of grain size less than 10 μm is observed in both the BM and CGHAZ specimens. However, in CGHAZ-100 kJ/cm specimen, the grain size greater than 10 μm tends to maintain a continuous fluctuation until the grain size exceeds 40 μm. Undoubtedly, the effective grain size increases obviously with the increase of heat input.

In addition, it is worth noting that the average value of effective grain size in the detected microzone is the smallest in BM, which is only ~1.76 μm. With the increase of heat input, the average value reach ~2.83 μm (25 kJ/cm) and ~6.35 μm (100 kJ/cm), respectively. The average value at 100 kJ/cm is twice as high as that at 25 kJ/cm, and the minimum and maximum values also show the similar trends. It can be seen that higher heat input has more effect on the effective grain size than that of the lower heat input.

Figure 9 shows the local misorientation average angles of BM and simulated CGHAZ based on EBSD technology. As can be seen from Fig. 9, the local misorientation average angles are mainly concentrated in the range of 1~2° (see Fig. 9a–c) in both the BM and CGHAZ specimens. It is worth noting that the values of 4~5° observed in BM are greater than that in CGHAZ (see Fig. 9d), especially that the values of 5° are almost zero in CGHAZ-100 kJ/cm (see Fig. 9c). Local misorientation average angle can indirectly reflect the defects in crystals, and is proportional to the dislocation density. It can be seen that the dislocation density in BM is higher than that in CGHAZ with different heat inputs.

3.4 Submicrostructure and Precipitation

The bright field images of submicrostructure of BM and simulated CGHAZ under TEM are shown in Fig. 10. As can be seen, the tempered lath bainite of BM is shown in Fig. 10a. After the welding thermal cycle, the submicrostructure of the BM changes in different degrees. At low heat input of 25 kJ/cm, the lath bainite is more obvious with massive precipitation of intergranular carbides due to the quicker cooling rate as shown in Fig. 10b, and the tempered lath bainite tends to be coarse due to the influence of higher heat input of 100 kJ/cm as shown in Fig. 10c. With the increase of heat input, the significant difference of submicrostructure lies in the coarse lath bainite and the intergranular carbides. The carbide precipitations between bainite laths are dissolved more or less in BM due to the tempered treatment. Besides, a large number of dislocation networks can be observed in both the BM and simulated CGHAZ specimens. Although

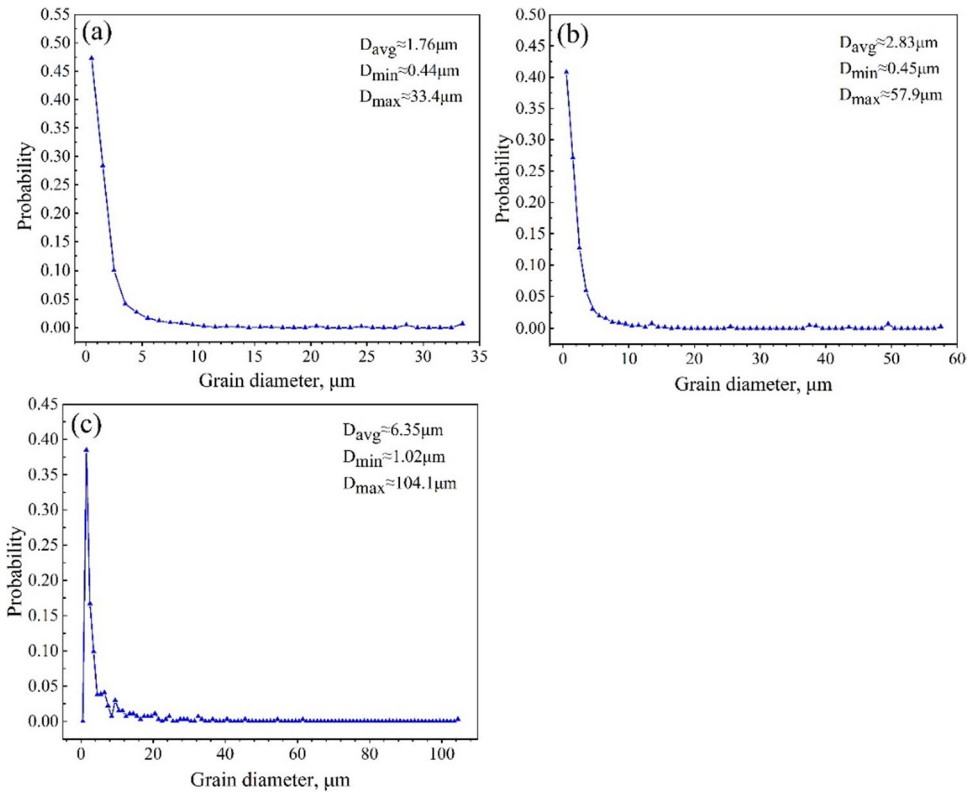

Fig. 8 Effective grain size of the BM and simulated CGHAZ based on EBSD technology. **a** BM; **b** 25 kJ/cm; **c** 100 kJ/cm

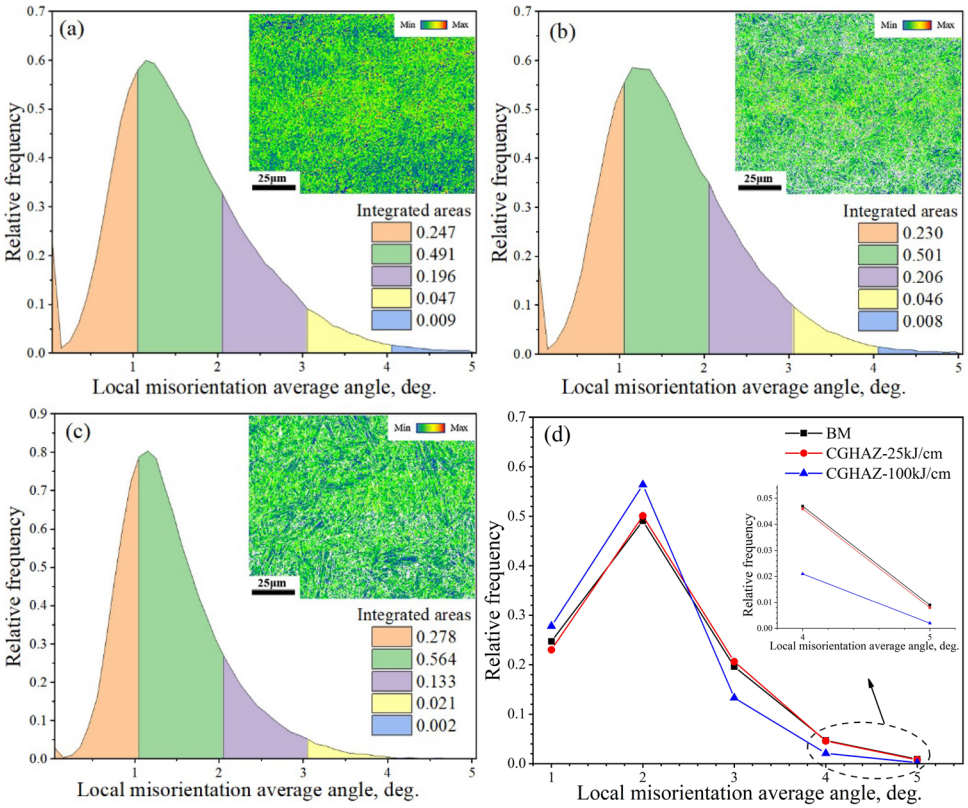

Fig. 9 Local misorientation average angles of BM and simulated CGHAZ based on EBSD technology. **a** BM; **b** CGHAZ-25 kJ/cm; **c** CGHAZ-100 kJ/cm. **d** Distribution of local misorientation average angles. The integrated areas of the segments reflect the distribution of the local misorientation average angles

the observation is in a microregion, it is sufficient to confirm that the dislocation can contribute greatly to the strength of matrix.

In order to verify whether the composition of carbides in CGHAZ is related to M-A constituents, selected area diffraction (SAD) analysis by TEM was carried out and the results are shown in Fig. 11. The diffraction position was performed on a typical precipitation phase as shown in Fig. 11a, and the SAD results are shown in Fig. 11b. It can be seen that the [002] direction of body-centered cube and the [-220] direction of face-centered cube agree with the results of SAD calibration. Therefore, it is not difficult to infer that the detected zone is a typical M-A constituent. Block or lath M-A constituents etched with LePera reagent are mainly precipitated at grain boundaries (Fig. 11d), which is basically consistent with the results as shown in Fig. 10c.

4 Discussion

4.1 Analysis of Microstructure in BM and CGHAZ

The microstructure of refined TLB as shown in Fig. 1a is critical to the basic mechanical properties of BM. Sanz et al. pointed out that the fine-grain strengthening method is the best way to ensure both the strength and toughness of matrix by investigating the effect of thermomechanical treatment and coiling temperature on the strengthening mechanism in low carbon steels microalloyed with niobium [23]. According to the process of industrial trial production, the refined microstructure of BM is ensured by the two-stage rolling process: the billet was deformed heavily in the austenite recrystallization regions (1100 ℃~ 1150℃) during the first rolling stage, and a large number of deformation bands were accumulated during the second rolling process of non-recrystallization temperature ranges (850~900℃), which provides more nucleation sites for subsequent phase transformation. Besides, the low-temperature tempering treatment further ensures the tempered lath bainite as shown in Fig. 1a. Compared with the complete martensite microstructure of high strength steel in other references, the strength and toughness are ensured by the refined lath bainite microstructure [14].

CGHAZ is known as the weakest position near the welded joint. For the single-pass welding process, the welding thermal cycle means that CGHAZ has undergone a complete austenitizing process and a solid-phase transformation process. This continuous cooling process is generally only affected by the welding heat input (related to the welding current, voltage and welding speed). Due to the short austenitizing time and fast cooling rate at low heat input, the austenitizing process of refined lath bainite is not sufficient. The interlocking lath microstructure is easy to retain inside the prior austenite grains under the influence of microstructure

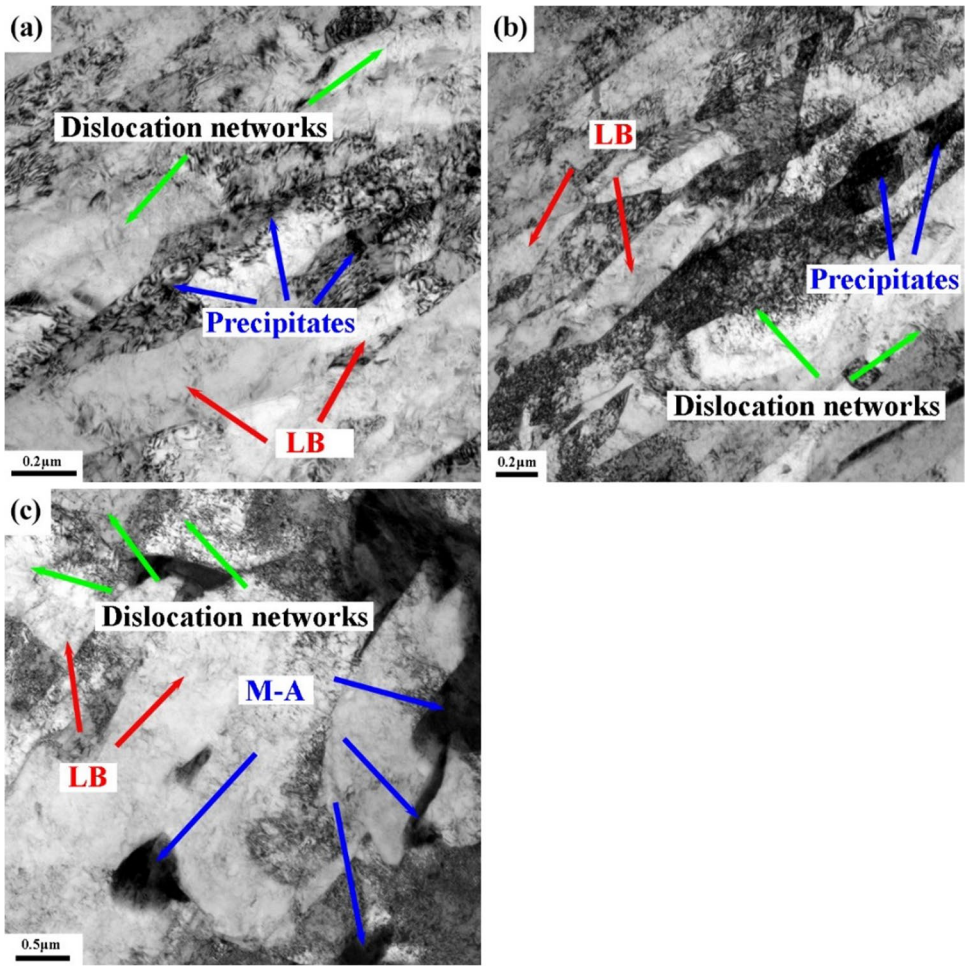

Fig. 10 Bright field TEM micrograph of the BM and simulated CGHAZ. **a** BM; **b** CGHAZ-25 kJ/cm; **c** CGHAZ-100 kJ/cm. M-A, martensite-austenite constituent; LB, lath bainite

heredity of BM. In addition, the granular bainite (GB) is also easy to be formed due to insufficient diffusion of partial carbon atoms during the continuous cooling process (as shown in Fig. 1b). The joint effect of granular bainite and residual lath bainite leads to an insignificant reduction of the high-angle boundaries. This is the main reason why the difference of boundary misorientation between 25 kJ/cm and BM is small (as shown in Fig. 6a and b). However, with the increase of heat input, the grain coarsening phenomenon is serious due to the long residence time of austenitizing at high temperature and slow cooling rate (as shown in Fig. 1c). At the same time, the lath bainite inside the prior austenite grain is easy to transform into more ferrite phase and a small amount of granular bainite due to the sufficient atomic diffusion under high heat input conditions. Therefore, the content of high-angle boundary decreases, which can explain the deterioration of impact performance of CGHAZ at high heat input conditions [16].

In addition, from the microstructure of the simulated CGHAZ-25 kJ/cm and CGHAZ-100 kJ/cm specimens, it can be seen that the prior austenite grains in CGHAZ-25 kJ/cm specimen are divided into many packets with high-angle boundaries (see in Fig. 6b). This chaotic lath microstructure is conducive to the improvement of impact toughness. However, due to the influence of high heat input of 100 kJ/cm, the coarse austenite grains are obvious in CGHAZ, and a large number of packets with similar crystallographic misorientation occur inside the austenite grains (see in Fig. 6c). Compared with the CGHAZ-25 kJ/cm specimen, the coarse austenite grains in CGHAZ provide a wide space for the formation of shear-mechanism bainite under the heat input of 100 kJ/cm, which may explain the formation of more high-frequency similar misorientation as shown in Fig. 6c. The multidirectional bainites with similar crystallographic orientation as shown in Fig. 2 by CSLM are related to the similar habit plane of shear nucleation, which is also consistent with the above analysis [24].

4.2 Analysis of Impact Toughness in BM and CGHAZ

The impact test results show that the CGHAZ toughness decreases generally especially for high heat input of 100 kJ/cm during the welding thermal cycles. Three factors such as inclusions, M-A constituents, and high-angle boundaries

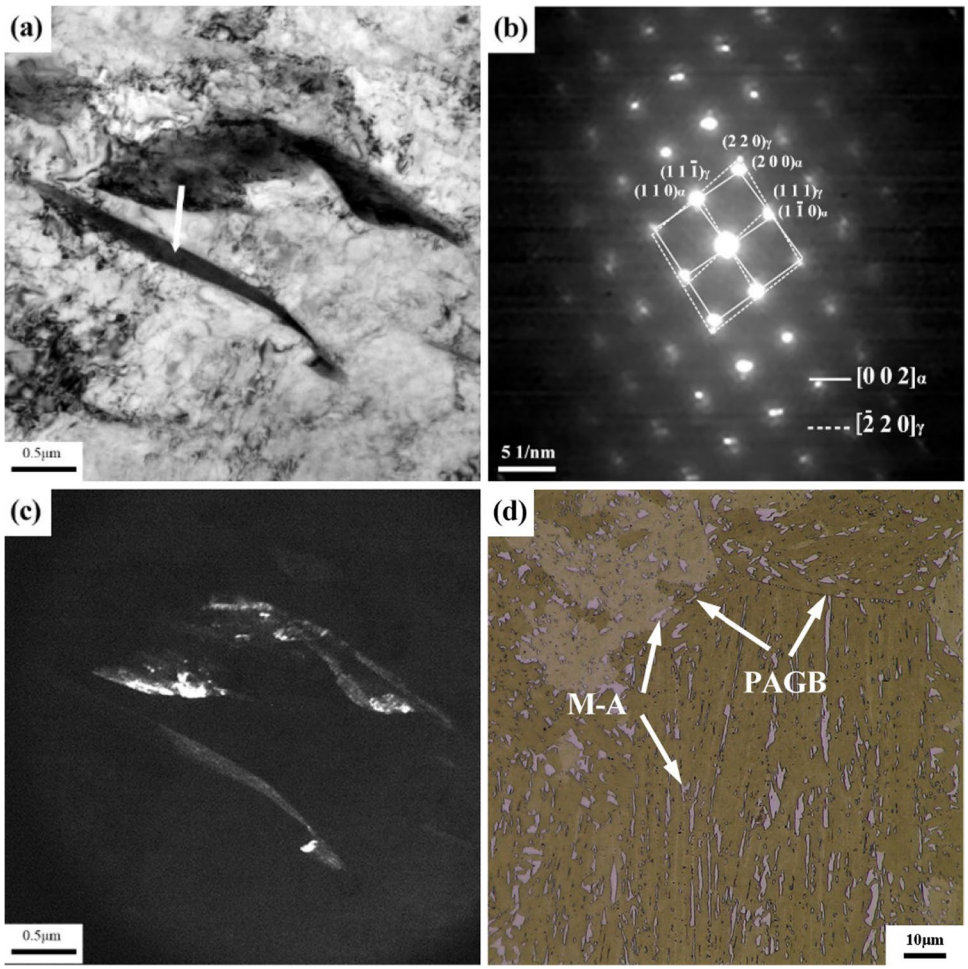

Fig. 11 Martensite–austenite (M-A) constituent in simulated high heat input CGHAZ-100 kJ/cm. **a** Bright field, **b** The corresponding selected area diffraction (SAD) pattern. **c** Dark field corresponding to **a**. The white arrow in **a** is the SAD analysis position. **d** Optical micrograph of M-A constituent etched with LePera reagent

in this investigated steel affect the impact properties comprehensively and are crucial to the formation of crack [7, 15, 18].

For inclusions, it is worth mentioning that most of the inclusions in the matrix are formed in the melting process with high melting point and good stability. Therefore, no matter in the tempering treatment or welding thermal cycle, such inclusions are difficult to decompose and change their properties but remain in the matrix [25, 26]. Although some inclusions are observed in the fractograph of BM as shown in Fig. 4b, the dimples are still more dense and the impact performance is still better than that of CGHAZ. Therefore, inclusions may not be the main reason for the decreasing toughness of CGHAZ than BM. They only provide a fair and favorable crack initiation condition for both the BM and CGHAZ.

For M-A constituents, Fig. 5 shows that the initiation of some cracks originates from the carbides or M-A constituents. Compared with the BM, larger M-A constituents (as shown in Fig. 10c) were observed in CGHAZ-100 kJ/cm, which indicates that a favorable condition for crack initiation can be provided. Bonnevie et al. divided the M-A constituents into three categories based on low-carbon microalloyed steel: one is complete twinning martensite with high dislocation density, the other is complete retained austenite with stacking defect, and the third is mixed constituents with austenite and martensite [27]. Figure 11 shows that the M-A constituents formed under high heat input of 100 kJ/cm are typical mixture of martensite and austenite, which is consistent with the third view of Bonnevie et al. This indicates that the formation of M-A constituent in the welding thermal cycle is directly related to the stability of prior austenite. Under high heat input conditions, the cooling rate slows down especially from the temperature of 800 to 500℃. This provides a dynamic condition for the retention of the prior austenite phase, and the short-range diffusion of carbon atoms results in the occurrence of carbon segregation, which is necessary for the formation of M-A constituents. The carbon enrichment during the phase transformation can significantly improve the stability of the residual austenite and reduce the initial martensite temperature in local regions [18]. Once the M-A constituent is formed, it will inevitably tend to induce apparent stress concentration at the interface. When the internal stress exceeds the strength

limit, the micropores will be formed, leading to the initiation source of microcracks due to the debonding mechanism preferentially [28].

For high-angle boundaries, the most obvious change after welding thermal cycle is the distribution of high-angle boundaries inside the prior austenite grains according to the results in Figs. 6 and 7. The prior austenite grains of the BM are mainly composed of high-angle boundaries. However, the interior of an individual austenite grain of CGHAZ-100 kJ/cm specimen is mainly occupied by more low-angle boundaries less than 15°. This means that the high-angle boundaries in prior austenite grains decrease significantly. Related literatures pointed out that the crack propagation can be arrested efficiently by the high-angle boundaries. However, the low-angle boundaries never result in an obvious deviation of the cleavage microcrack [29, 30]. It can be seen that the low-angle boundaries in the prior austenite grains may be responsible for the negative effect on the impact toughness of CGHAZ. After being subjected to different heat input welding energy, the content of high-angle boundaries in CGHAZ decreases significantly, which greatly reduces the inhibiting effect on the crack propagation. As shown in Fig. 3, the crack propagation energy contributes greatly to the total impact energy. Therefore, the total impact absorbed energy shows better in BM because of the positive effect of high-angle boundaries on crack propagation. The impact toughness decreases significantly at high heat input of 100 kJ/cm, which is closely related to the decreasing content of high-angle grain boundaries.

In addition, the results in Fig. 9 indicate that the dislocation density of BM seems higher than that of CGHAZ. Although higher dislocation density can bring more stress concentration to cause crack initiation easily, the impact performance of BM still shows better than CGHAZ, which is mainly related to the small effective grains and higher content of high-angle boundaries in BM. The effective grains are considered as key factors to influence the impact toughness because of the inhibiting effect of crack propagation by high-angle boundaries [15, 16, 19, 31–34]. Usually, the misorientaiton greater than 50° is generally considered as the prior austenite boundary [5]. From Fig. 1, the austenite grain size increases generally after welding thermal cycles, which in nature decreases the area fraction of high-angle austenite grain boundaries. As a result, the decreasing frequency of high-angle boundaries is observed as shown in Fig. 7. On the one hand, the coarse microstructure leads to the decrease in the proportion of high-angle boundaries. On the other hand, the precipitates of granular carbides provide favorable conditions for the initiation of cracks, which is not conducive to the impact energy. In addition, during the welding process of high heat input of 100 kJ/cm, the low-angle boundaries are increased, which is not conducive to the arrest behavior of cracks. In the process of crack propagation as shown in Fig. 5, when the crack tip extends to the grain boundary, it will either choose a transgranular fracture mode, or change the direction of crack propagation or even stop propagation, which largely depends on the percentage of high-angle boundaries. In essence, the smaller the effective grain is, the higher the grain boundary fraction has, and the higher the frequency of high-angle boundaries tends to be. Therefore, the effective grains with high-angle boundaries do play a certain role on inhibiting the crack propagation.

According to the results of this experiment, several forms of cracks during the impact process can be assumed: one is complete transgranular fracture; secondly, the crack originates from the stress concentration sites (such as M-A islands, carbides, or inclusions) and gradually extends to the grain boundaries. Thirdly, the crack propagation terminates inside the grains. The schematic diagram of the crack initiation and propagation process was drawn as shown in Fig. 12. For the impact process of BM and low heat input of 25 kJ/cm, the crack propagation path is repeatedly deflected or continuously constrained by the high-angle boundaries. However, for high heat input of 100 kJ/cm, the crack propagation path is almost straight, resulting in massive cleavage planes, which is not beneficial to the crack arrest behavior.

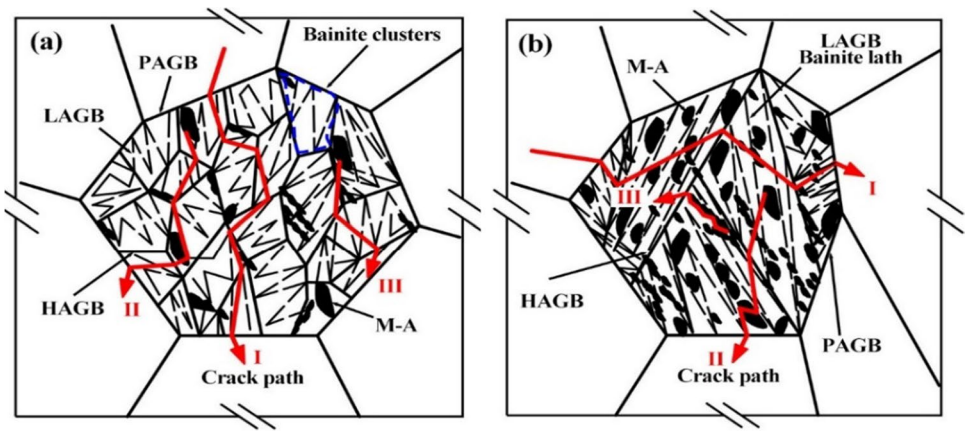

Fig. 12 Schematic diagram of crack initiation and propagation process. **a** BM; **b** CGHAZ-100 kJ/cm. The Roman numbers I, II, III represent the crack propagation paths. HAGB, high-angle grain boundary; LAGB, low-angle grain boundary; PAGB, prior austenite grain boundary; M-A, martensite-austenite constituents. The blue dotted box in **a** indicates a bainite cluster

Therefore, the impact toughness of CGHAZ during high heat input energy decreases significantly.

5 Conclusions

In this paper, the microstructure and impact toughness between BM and simulated CGHAZ with different heat inputs in a 690 MPa ultra-low-carbon high-strength microalloyed steel were characterized and analyzed. The following conclusions were drawn:

A favorable impact test value of ~140 J at − 20℃ maintains in CGHAZ under the heat input of 25 kJ/cm. With the increase of heat input to 100 kJ/cm, the impact energy of CGHAZ at − 20℃ still reaches ~40 J. The inclusions are not the main reason for the decreasing toughness of CGHAZ versus BM, because the inclusions are formed in the melting process and they only provide a fair and favorable condition for crack initiation in both the BM and CGHAZ specimens. The M-A constituents detected in CGHAZ are the typical complex phase of martensite and austenite, which can be as the crack initiation sources during the impact process. More low-angle boundaries and the less frequency of high-angle boundaries in the prior austenite grains due to the high heat input are not conducive to the crack arresting behavior. Because of the restraining effect of high-angle boundaries on crack propagation, the contribution of crack propagation to total impact absorbed energy is greater than that of crack initiation. The interlocking lath microstructure is easy to retain inside the prior austenite grains under the condition of low heat input of 25 kJ/cm due to the influence of microstructure heredity of BM, which ensures that the CGHAZ toughness of 25 kJ/cm does not deteriorate significantly. For 690 MPa ultra-low-carbon high-strength microalloyed steels, effective microstructure refinement of BM is important to improve the impact toughness of CGHAZ during the high heat input welding process.

Author Contribution Yulong Yang: conceptualization, methodology, formal analysis, writing—original draft, writing—review and editing, data curation. Xiao Jia, Yaxin Ma: investigation, validation, methodology, formal analysis. Ping Wang: methodology, validation, resources, supervision. Fuxian Zhu: methodology, funding acquisition, supervision, resources.

Funding This work is strongly supported by the fundamental research funds for the central universities of China (No. N2007009) and the major industrial projects of science and technology plan of Liaoning Province, China (No. 2019JH1/10100014).

Data Availability The raw/processed data required to reproduce these findings cannot be shared at this time as the data also forms part of an ongoing study.

Declarations

Conflict of Interest The authors declare no competing interests.

References

1. Uemori R, Inoue T, Ichikawa K et al (2012) Steels for marine transportation and construction, Nippon Steel Technical Report:37–46
2. Xi X, Wang J, Chen L et al (2020) On the role of Cu addition in toughness improvement of coarse grained heat affected zone in a low carbon high strength steel. J Mater Sci 55:10863–10877
3. Cao R, Li J, Liu DS et al (2015) Micromechanism of decrease of impact toughness in coarse-grain heat-affected zone of HSLA steel with increasing welding heat input. Metall Mater Trans A 46:2999–3014
4. Hu J, Du LX, Wang JJ et al (2013) Effect of welding heat input on microstructures and toughness in simulated CGHAZ of V-N high strength steel. Mater Sci Eng A 577:161–168
5. Lan L, Kong X, Chang Z et al (2017) Microstructure, composition, and impact toughness across the fusion line of high-strength bainitic steel weldments. Metall Mater Trans A 48:4140–4153
6. Kang YJ, Jeong SH, Kang JH et al (2016) Factors affecting the inclusion potency for acicular ferrite nucleation in high-strength steel welds. Metall Mater Trans A 47:2842–2854
7. Gordienko AI, Derevyagina LS, Malikov AG et al (2020) The effect of the initial microstructure of the X70 low-carbon microalloyed steel on the heat affected zone formation and the mechanical properties of laser welded joints. Mater Sci Eng A 797:2–8
8. Xiong ZH, Liu SL, Wang XM et al (2015) The contribution of intragranular acicular ferrite microstructural constituent on impact toughness and impeding crack initiation and propagation in the heat-affected zone (HAZ) of low-carbon steels. Mater Sci Eng A 636:117–123
9. Wan XL, Wei R, Wu KM (2010) Effect of acicular ferrite formation on grain refinement in the coarse-grained region of heat-affected zone. Mater Charact 61:726–731
10. Wang X, Wang C, Kang J et al (2020) Improved toughness of double-pass welding heat affected zone by fine Ti–Ca oxide inclusions for high-strength low-alloy steel. Mater Sci Eng A 780:2–10
11. Lan L, Qiu C, Zhao D et al (2013) Effect of reheat temperature on continuous cooling bainite transformation behavior in low carbon microalloyed steel. J Mater Sci 48:4356–4364
12. Haslberger P, Holly S, Ernst W et al (2018) Microstructure and mechanical properties of high-strength steel welding consumables with a minimum yield strength of 1100 MPa. J Mater Sci 53:6968–6979
13. Xie H, Du LX, Hu J et al (2015) Effect of thermo-mechanical cycling on the microstructure and toughness in the weld CGHAZ of a novel high strength low carbon steel. Mater Sci Eng A 639:482–488
14. Kwak K, Mayama T, Mine Y et al (2016) Micro-tensile behaviour of low-alloy steel with bainite/martensite microstructure. ISIJ Int 56:2313–2319
15. Lan L, Qiu C, Zhao D et al (2011) Microstructural characteristics and toughness of the simulated coarse grained heat affected zone of high strength low carbon bainitic steel. Mater Sci Eng A 529:192–200
16. Cui B, Peng Y, Zhao L et al (2016) Effect of heat input on microstructure and toughness of coarse grained heat affected zone of Q890 Steel. ISIJ Int 56:132–139

17. Shi M, Zhang P, Zhu F (2014) Toughness and microstructure of coarse grain heat affected zone with high heat input welding in Zr-bearing low carbon steel. ISIJ Int 54:188–192
18. Lan L, Qiu C, Zhao D et al (2012) Analysis of martensite–austenite constituent and its effect on toughness in submerged arc welded joint of low carbon bainitic steel. J Mater Sci 47:4732–4742
19. Lan L, Qiu C, Zhao D et al (2012) Analysis of microstructural variation and mechanical behaviors in submerged arc welded joint of high strength low carbon bainitic steel. Mater Sci Eng A 558:592–601
20. Li C, Wang Y, Han T et al (2010) Microstructure and toughness of coarse grain heat-affected zone of domestic X70 pipeline steel during in-service welding. J Mater Sci 46:727–733
21. Lambert-Perlade A, Gourgues AF, Besson J et al (2004) Mechanisms and modeling of cleavage fracture in simulated heat-affected zone microstructures of a high-strength low alloy steel. Metall Mater Trans A 35:1039–1053
22. Ramachandran DC, Moon J, Lee C-H et al (2021) Role of bainitic microstructures with M-A constituent on the toughness of an HSLA steel for seismic resistant structural applications. Mater Sci Eng A 801:2–11
23. Sanz L, Pereda B, López B (2017) Effect of thermomechanical treatment and coiling temperature on the strengthening mechanisms of low carbon steels microalloyed with Nb. Mater Sci Eng A 685:377–390
24. Poorhaydari K, Patchett BM, Ivey DG (2006) Transformation twins in the weld HAZ of a low-carbon high-strength microalloyed steel. Mater Sci Eng A 435–436:371–382
25. Yang C, Luan Y, Li D et al (2019) Effects of rare earth elements on inclusions and impact toughness of high-carbon chromium bearing steel. J Mater Sci Technol 35:1298–1308
26. Chai F, Yang CF, Su H et al (2009) Effect of magnesium on inclusion formation in Ti-killed steels and microstructural evolution in welding induced coarse grained heat affected zone. J Iron Steel Res Int 16:69–74
27. Bonnevie E, Ferrière G, Ikhlef A et al (2004) Morphological aspects of martensite–austenite constituents in intercritical and coarse grain heat affected zones of structural steels. Mater Sci Eng A 385:352–358
28. Mohseni P, Solberg JK, Karlsen M et al (2013) Cleavage fracture initiation at M-A constituents in intercritically coarse-grained heat-affected zone of a HSLA steel. Metall Mater Trans A 45:384–394
29. Lambert A, Garat X, Sturel T et al (2000) Application of acoustic emission to the study of cleavage fracture mechanism in a HSLA steel. Scripta mater 43:161–166
30. Lambert-Perlade A, Gourgues AF, Pineau A (2004) Austenite to bainite phase transformation in the heat-affected zone of a high strength low alloy steel. Acta Mater 52:2337–2348
31. Chen L, Nie P, Qu Z et al (2020) Influence of heat input on the changes in the microstructure and fracture behavior of laser welded 800MPa grade high-strength low-alloy steel. J Manuf Process 50:132–141
32. Kim BC, Lee S, Kim NJ et al (1991) Microstructure and local brittle zone phenomena in high-strength low-alloy steel welds. Metall Mater Trans A 22:139–147
33. Gutiérrez I (2013) Effect of microstructure on the impact toughness of Nb-microalloyed steel: generalisation of existing relations from ferrite–pearlite to high strength microstructures. Mater Sci Eng A 571:57–67
34. Isasti N, Jorge-Badiola D, Taheri ML et al (2014) Microstructural features controlling mechanical properties in Nb-Mo microalloyed steels. Part I: Yield strength, Metall Mater Trans A 45:4960–4971